Rock and Soil Mechanics 2025 46(10): 3117−3131 ISSN 1000−7598
https: //doi.org/10.26599/RSM.2024.94300230 journal homepage: rocksoilmech.whrsm.ac.cn

Effect of mineral composition on soil-water characteristics of red soil

SUN Yin-lei[1], LI Zhi-fei[1], CHEN Yan-ge[1], DU Qing-ru[1], TIAN Ke-meng[1], CHEN Jun-lei[1], ZHANG Xian-wei[2]

1. School of Architecture and Planning, Yunnan University, Kunming, Yunnan 650500, China

2. State Key Laboratory of Geomechanics and Geotechnical Engineering Safety, Institute of Rock and Soil Mechanics, Chinese Academy of Sciences, Wuhan, Hubei 430071, China

Abstract: Mineral composition is one of the critical factors regulating the soil-water characteristic curve (SWCC) and micro-pore structure in red soil. The purpose of this study is to analyze the mechanism of mineral composition on the soil-water characteristics of red soil from the microstructural level. The response curve method was employed to systematically evaluate the effects of different mineral compositions on matrix suction, with three key ratios selected for investigation. Using the contact filter paper method, SWCCs were obtained for humidified soil samples with three distinct mineral proportions. Additionally, scanning electron microscopy and mercury intrusion porosimetry were utilized to reveal pore microstructure and distribution characteristics. The results indicate that the regression model constructed using Box-Behnken design demonstrates significant effects of kaolinite and illite on matric suction during variance fitting analysis, whereas montmorillonite exhibits no significant influence. The interaction between kaolinite and illite has a much greater impact on matric suction than the interaction between kaolinite and montmorillonite when a specific variable is fixed. Furthermore, the influence of mineral composition on the SWCC is minimal in the near-saturation and residual regions, where the curve remains relatively flat. In the transition region, the slope of the SWCC increases significantly for samples with high kaolinite content, while the slope is relatively small for samples rich in the other two mineral components. Regarding microstructure, samples with high kaolinite and illite content exhibit uneven sand particle boundaries, large flocculated structures with cross-distribution, and a rich macroporous structure. In contrast, the other two groups of samples display a relatively loose dispersed structure. Moreover, there is a strong correspondence between the dominant pore size range in the pore size distribution curve and the transition region of the SWCC, further validating the profound influence of mineral composition on the soil-water characteristics of red soil.

Keywords: mineral composition; response surface methodology; soil-water characteristics; pore structure

1 Introduction

The soil-water characteristic curve (SWCC) is a fundamental curve that delineates the relationship between suction and water content (or saturation) in unsaturated soils[1-2]. It serves not only as a basic constitutive relationship in unsaturated soil mechanics but also profoundly illustrates the critical influence of soil pore structure on mechanical properties[3-4]. This curve is intrinsically linked to key properties of unsaturated soils, including permeability, strength, and volumetric changes. Furthermore, it acts as an essential bridge connecting theoretical frameworks, experimental testing, and predictive methodologies, playing an indispensable role in understanding and forecasting the coupled hydro-mechanical-chemical processes in unsaturated soils[5].

The soil-water characteristic curve is influenced by a multitude of factors that can be categorized into intrinsic and extrinsic factors (see Fig.1). Intrinsic factors encompass mineral composition, pore structure, particle size distribution, dry density, initial water content, and soil fabric. Extrinsic factors include stress history, confining pressure, dry-wet cycles, freeze-thaw effects, and temperature variations, among others[6-7]. The influence of various factors on soil-water characteristic curves has been extensively investigated by scholars globally. Tang et al.[8] demonstrated that particle size gradation has a significant influence on the soil-water characteristic curve. Specifically, larger particle sizes exhibit a linear "stepped" distribution, whereas smaller particle sizes tend to display a more linear pattern. Furthermore, particle size composition is closely associated with the hysteresis and intake values of the soil-water characteristic curve[9-10]. In well-graded soils, particles of varying sizes interlock with one another, forming a complex pore structure. This results in the soil-water characteristic curve presenting a more intricate morphology[11]. The macroscopic physical and mechanical properties of soil reflect, to some extent, the external manifestation of its internal microstructure[12]. Chen et al.[13] revealed that variations in initial compaction conditions markedly affect the mechanical and hydraulic characteristics of in-situ granite residual soil subgrade, fundamentally due to changes in pore structure and soil-water characteristics. Furthermore, microstructural analysis reveals that soil-water characteristics are predominantly governed by pore distribution. Specifically, larger pores facilitate easier water discharge during drainage, resulting in a lower air intake value and a flatter soil-water

Received: 13 April 2025 Accepted: 30 May 2025
This work was supported by the National Natural Science Foundation of China (42102303, 52568054, 42372313, 42177148), the General Program of Natural Science Foundation of Yunnan Province (202401CF070174), the Xingdian Talent Support Program (C619300130) and the Open Research Fund of Key Laboratory of Flood & Drought Disaster Defense, the Ministry of Water Resources (wx20241100518).
First author: SUN Yin-lei, male, born in 1986, PhD, Associate Professor, mainly engaged in research on the properties of special soils and other aspects. E-mail: sunylei@ynu.edu.cn
Corresponding author: ZHANG Xian-wei, male, born in 1982, PhD, Professor, mainly engaged in fundamental research on special soil mechanics and applied research on disaster management and control. E-mail: xwzhang@whrsm.ac.cn

characteristic curve[14]. Consequently, there exists a corresponding relationship between the pore distribution curve and the soil-water characteristic curve[15], enabling the prediction of distinct soil-water characteristic curves under varying pore conditions via the proposed model[16-17]. Wang et al.[18] and Cui et al.[19] examined the effects of dry-wet and freeze-thaw cycles on SWCCs, finding that increased cycle numbers reduce water retention capacity, leading to noticeable differences in SWCCs across different cycle counts. Luo et al.[20] experimentally determined that the intake air value of sandy gravel soil exhibits a linear correlation with vertical stress but a hyperbolic relationship with the slope of the SWCC. Moreover, beyond a certain level of vertical stress, its impact on the intake air value becomes negligible[21]. Pham et al.[22-23] explored the effect of temperature on SWCCs, revealing that rising temperatures weaken matrix suction and decrease water retention. However, although there have been many studies involving the influencing factors of the soil-water characteristic curve, as an important component of soil, the research on the influence of mineral components on the soil-water characteristic curve of red soil lags behind relatively. Due to the small particle size and relatively large specific surface area of mineral components, they exhibit complex dispersion, ion exchange, plasticity and expansion and contraction when interacting with water molecules. Coupled with the strict requirements of research methods and the high consumption of quantitative analysis resources, the current exploration of the influence of mineral components on the soil-water characteristic curve of laterite is still scarce, and the existing research is only limited to the influence of a single mineral component. This provides an opportunity for further studying the influence of mineral composition on the soil-water characteristic curve of laterite. The exploration carried out in this aspect in this study has certain academic value and reference significance.

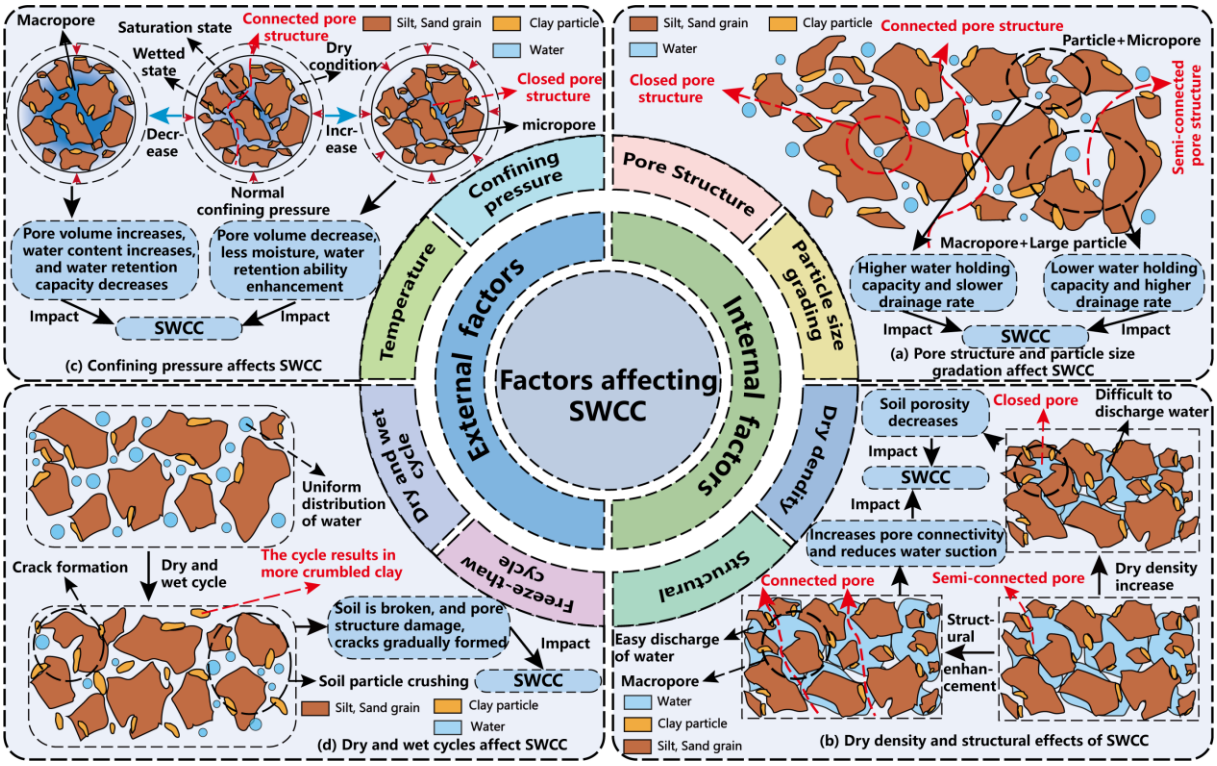


Fig.1 Influence of various factors on soil-water characteristic curves

In this study, red soil samples containing diverse mineral types and varying contents were prepared. The response surface methodology was employed to examine the impact of different mineral ratios on the matric suction of red soil, with three critical ratios being identified. By utilizing soil-water characteristic curve fitting, mercury intrusion porosimetry, and scanning electron microscopy analysis, the effects of varying mineral compositions on the soil-water characteristics and pore structure of red soil were comprehensively investigated. This research elucidates the influence mechanism of mineral composition on red soil properties from the perspectives of mineralogy and microstructure. The technical approach adopted in this study is illustrated in Fig.2.

2 Materials and methods

2.1 Determination of sand content

The soil samples for testing were collected from Chenggong District, Kunming City, and laboratory analysis confirmed the soil type as red clay. During the soil sample collection stage, the extracted soil samples were dried, crushed, and passed through a 2 mm sieve to prepare them for subsequent experiments. Additionally, the clay mineral content was further analyzed. During sample preparation, the sand content in the clay minerals was increased from 0 to 70%, and the configuration was carried out at intervals of

5%, with standard quartz sand used. The soil samples were prepared with a dry density of 1.7 g/cm³, moisture content of 17%, and compaction degree of 95%. Loose soil samples were compacted into cutting ring specimens measuring 5 cm in diameter and 2 cm in height using the static pressure method, with two parallel specimens prepared for each sand content level. Subsequently, the matrix suction of the soil samples with varying sand contents was measured using the contact filter paper method (see Fig.3). The filter paper used in this experiment was domestic "Double Circle" brand No. 203 quantitative filter paper, characterized by a slow filtration rate, a diameter of 70 mm, and an ash content of 0.01%.

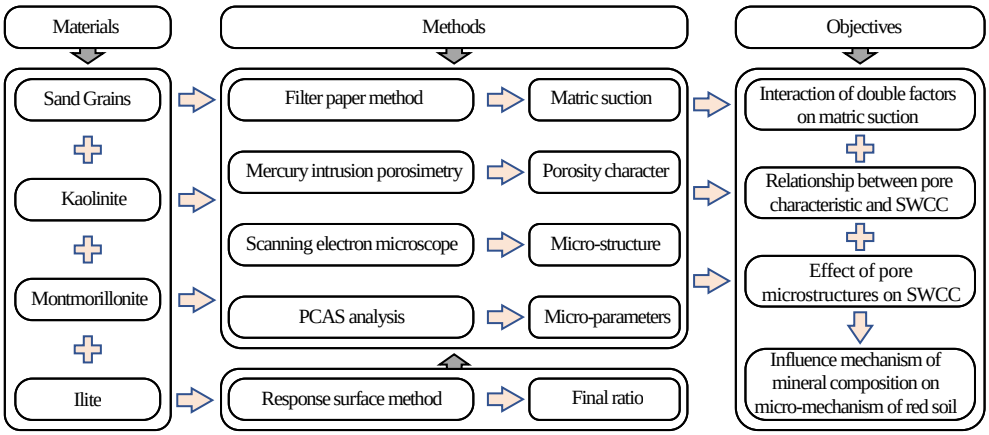


Fig.2 Technology roadmap

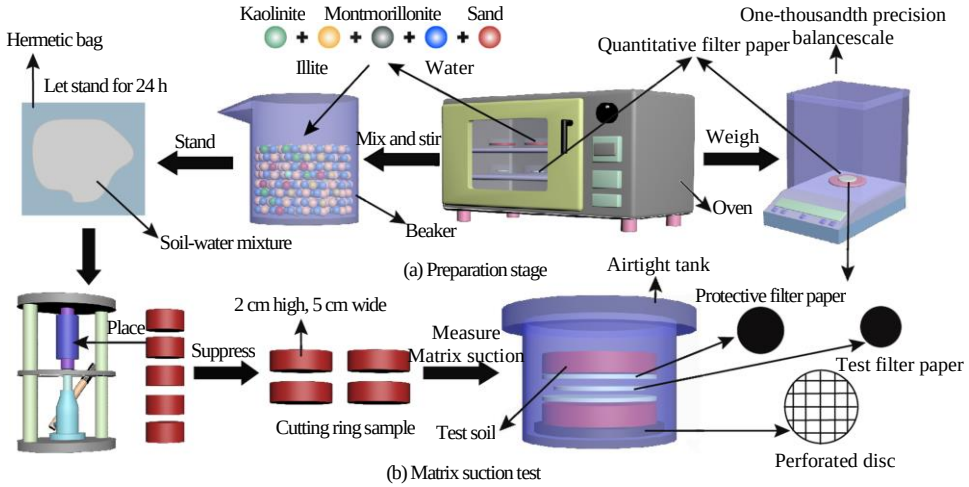


Fig.3 Test device schematic diagram

The procedures for conducting a matrix suction test are outlined as follows:

(1) Place the filter paper in a high-temperature oven for 12 h to determine the matrix suction of the soil sample under varying sand content conditions. Three pieces of dried filter paper were carefully retrieved with tweezers and positioned between two cutting ring soil samples. The upper and lower layers served as protective filter paper with a width of 5 cm, while the middle layer functioned as the test filter paper with a width of 4.5 cm, ensuring direct contact between the filter paper and the soil sample. The dry weight of the middle filter paper was measured using an analytical balance with one-thousandth accuracy. The two soil samples were securely sealed with waterproof tape and subsequently wrapped layer by layer with plastic film.

(2) Place the wrapped soil sample in a sealed glass container and subsequently transfer the sealed container to a 25 ℃ incubator for a period of 10 d. After the incubation period, retrieve the sample and use tweezers to carefully extract the centrally positioned test filter paper (to minimize exposure to ambient moisture, this procedure should be completed within 30 s). The wet weight of the filter paper was then measured using a balance with a precision of 0.001 g. The moisture content of the filter paper was calculated according to Eq.（1）, and the matrix suction of the excavated sample was determined using Eq.（2）.

$$w_{\mathrm{f}}=\left(\frac{m_2}{m_1}-1\right)\times 100\% \tag{1}$$

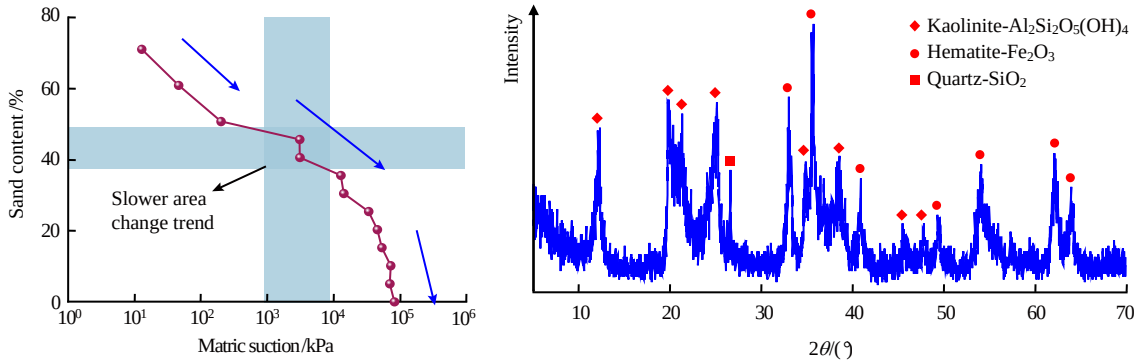
where m_1 represents the dry weight of the filter paper (g); m_2 denotes the wet weight of the filter paper (g); and w_{f} signifies the moisture content of the filter paper (%).

The governing equation[24] is:

$$\left.\begin{aligned}\lg S&=5.493-0.076w_{\mathrm{f}},\quad w_{\mathrm{f}}<47\%\\ \lg S&=2.470-0.012w_{\mathrm{f}},\quad w_{\mathrm{f}}\geqslant 47\%\end{aligned}\right\} \tag{2}$$

where S refers to matrix suction (kPa).

Based on the matrix suction test, the relationship curve between the sand content of the soil sample and the matrix suction is illustrated in Fig.4(a). As observed from the figure, as the sand content increases, the overall matric suction of the soil sample exhibits a downward trend, with a clear change pattern. Specifically, when the sand content ranges from 40% to 45%, further increases in sand content have minimal impact on the matric suction of the soil sample, to the extent that such changes can be considered negligible. Therefore, to minimize the influence of sand content on subsequent tests and control experimental variables, the sand content for this experiment was set at 40%.



(a) Plot of matrix suction and sand content (b) Analysis of laterite composition

Fig.4 Pre-experimental data

2.2 Response surface methodology (RSM)

Response surface methodology (RSM) is an advanced approach that integrates experimental design and mathematical modeling to optimize processes. By testing representative local points, RSM enables regression fitting of the functional relationship between factors and outcomes across the entire range, thereby determining the optimal levels for each factor. The quantitative analysis of kaolinite, montmorillonite, and illite in red soil was conducted using X-ray diffraction (see Fig.4(b)). In conjunction with a selected sand content of 40%, the final determined contents of kaolinite, montmorillonite, and illite were 30% to 42%, 0% to 12%, and 12% to 24%, respectively. For this experiment, the independent variables included the content of kaolinite powder (factor A), montmorillonite powder (factor B), and illite powder (factor C), each at three levels. To comprehensively analyze the influence of sample moisture content on matrix suction force, the matrix suction force at sample moisture contents of 10%, 15%, and 20% was selected as the response variable. A moisture content of 10% approximates the condition of red soil in a dry state, 20% corresponds to its saturated state, and 15% represents an intermediate condition. These three moisture levels effectively encompass the potential range of moisture content that red soil may experience under actual engineering conditions, thereby providing a more thorough understanding of how mineral composition affects matrix suction force. The test factors and their corresponding levels are presented in Table 1. The response surface analysis was performed using Design-Expert 10 software to investigate the impact of mineral composition on the suction force of the laterite matrix. In this study, the Box-Behnken design method was employed for experimental design within the software. The significance level of the model was established at 0.05. A quadratic polynomial model was utilized for regression fitting, and the model was subsequently validated and optimized through analysis of variance.

Table 1 Test factor and level of response surface method

Level	Factor A/%	Factor B/%	Factor C/%
−1	30	0	12
0	36	6	18
1	42	12	24

2.3 Measurement of soil water characteristic curve

Based on the content ranges of three mineral components established through the response surface methodology, soil samples with varying proportions of kaolinite powder, montmorillonite powder, illite powder, and sand particles were prepared. Water was added to the soil samples using a dropwise method to achieve moisture contents ranging from 5% to 23%, with increment of 1%. The water-soil mixtures were then sealed in bags for 24 h to ensure thorough contact and homogeneous mixing, preventing particle agglomeration. Static soil samples were subsequently molded into ring cutter specimens according to the parameters outlined in Section 2.1. Matrix suction tests were conducted following the specified procedure, evaluating the effects of different mineral component compositions.

To develop the soil-water characteristic curve model, the gravimetric water content of the soil sample was converted to volumetric water content using Eq.（3）.

$$\theta = \frac{\omega \rho_{\mathrm{d}}}{\rho_{\mathrm{w}}} \tag{3}$$

where θ is the volumetric moisture content of the soil

sample (%); ω is the mass moisture content of the soil sample (%); ρ_d is the dry density of the soil sample (g/cm^3); and ρ_w is the density of water (g/cm^3).

Based on the data of water content and matric suction, the Gardner (GA)[25], Van Genuchten (VG)[26], Fredlund & Xing (FX)[27], and the three-parameter Van Genuchten[28] models were utilized to fit the data. The corresponding fitting equations are as follows:

GA model:

$$\theta = \theta_r + \frac{\theta_s - \theta_r}{1 + (S/a)^n} \tag{4}$$

VG model:

$$\left.\begin{aligned} \theta &= \theta_r + \frac{\theta_s - \theta_r}{[1 + (S/a)^n]^m} \\ m &= 1 - \frac{1}{n} \end{aligned}\right\} \tag{5}$$

FX model:

$$\theta = \frac{\theta_s}{\{\ln[e + (S/a)^n]\}^m} \tag{6}$$

Three-parameter Van Genuchten model

$$\theta = \theta_r + \frac{\theta_s - \theta_r}{[1 + (Sa)^n]^m} \tag{7}$$

where θ_r denotes the residual volumetric water content (%); θ_s indicates the saturated volumetric moisture content (%); a is the parameter associated with the air entry value; n is the model parameter related to pore size distribution; and m is a model parameter associated with the overall symmetry of the curve.

2.4 Mercury injection testing

The mercury injection test, grounded in capillary action principles, quantifies the volume of mercury intruded into soil pores under varying external pressures. As external pressure increases, mercury can penetrate progressively smaller pore radii, eventually filling all accessible pores at sufficiently high pressures. The experiment involves measuring and recording the volume of mercury intruded at different pressures, from which pore diameters are calculated using Eqs.（2）and（3）. This process yields a curve representing the relationship between pore diameter and mercury volume. This curve can determine the situation that pores of different sizes are filled as pressure increases, thereby providing insights into the soil's pore size distribution. For the test, soil samples with optimal moisture content at each level were selected, ensuring that their dimensions (length, width, and height) did not exceed 15 mm. After undergoing drying and freezing, these samples were analyzed using a high-performance automatic mercury injection instrument (model: AutoPore IV 9510). The testing pressure range was set from 1.4 kPa to 206 kPa for low-pressure measurements and from 138 kPa to 413 640 kPa for high-pressure measurements.

2.5 Scanning electron microscopy analysis

Soil samples with dimensions (length, width, and height) less than 5 mm were selected from the cutting ring samples exhibiting optimal moisture content at each level for SEM analysis. The selected soil samples were subsequently dried and subjected to adhesive treatment[29], grinding, profiling, and gold sputtering. Finally, the prepared samples were analyzed under a scanning electron microscope (SEM, instrument model Regulus 8100) for imaging.

2.6 Extraction of feature parameters for pore structure characteristics

In the SEM test, to achieve a clearer image of soil particles, the darkest and brightest points in the image do not correspond to the extreme gray values. Therefore, Image Pro Plus (IPP) was utilized to process the gray value distribution of the SEM images obtained from the test using normal distribution (square equalization). A binary threshold was selected, resulting in a binarized image. The Pores and Cracks Analysis System (PCAS) was then employed to analyze the binarized image, extracting fundamental parameters such as porosity, perimeter, area, and orientation characteristics of the soil microstructure. Based on these basic parameters, equivalent parameters (average area, average perimeter, average major axis, average minor axis), dimensionless parameters (aspect ratio, roundness, shape coefficient), angular distribution, and probabilistic entropy were calculated.

3 Results and analysis

3.1 Response surface methodology analysis

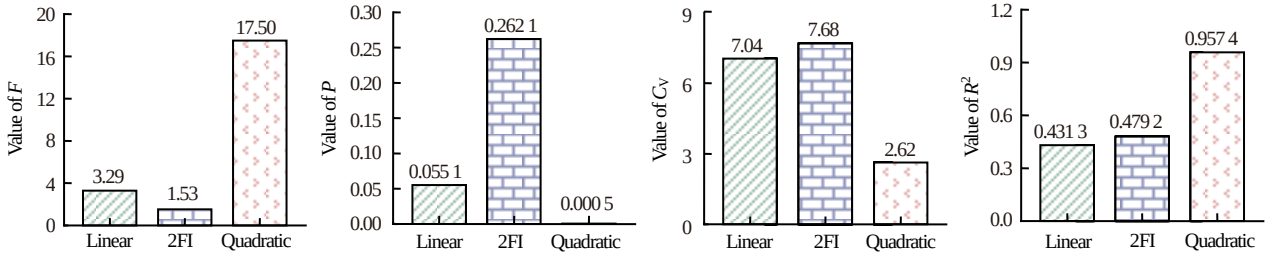
Based on the test factors of the response surface methodology (see Table 1), a total of 17 experimental groups were designed using the Box-Behnken design. The experimental design is presented in Table 2, which includes five zero-point repetition test groups. These groups are uniformly distributed near the center point of the experimental design to minimize experimental errors.

Design-Expert 13 software was utilized to conduct comprehensive model fitting analyses on the relationship between matric suction at moisture contents of 10%, 15%, and 20% and the three influencing factors. The most appropriate model was selected based on the model synthesis coefficients. Taking the matric suction at 10% moisture content as an example, fitting analyses were performed for the linear model, two-factor interaction model (2FI), and quadratic polynomial model. The corresponding comprehensive coefficient outputs are illustrated in Fig.5. As shown in the figure, among the three models, only the quadratic polynomial model exhibits a coefficient of determination (R^2) greater than 0.9, indicating high fitting reliability and minimal test error[30]. Additionally, the coefficients of variation (C_V) were all below 10%, further confirming the reliability and precision of the test results. The F-score measures a model's ability to interpret data variation; the higher the

valueis, the more significant the model is. The *P*-value assesses the statistical reliability of this significance, and a value below 0.05 is generally considered significant. In the figure, the *F*-value of the quadratic polynomial model is the highest, indicating that it can capture more changes in matrix suction caused by influencing factors. Combined with the *P*-value, it can be seen that the high *F*-value directly leads to a *P*-value less than 0.05, and its model is significant[31]. The linear model and the two-factor model are not significant. Therefore, a quadratic polynomial model is selected for fitting the matrix suction values of samples with different moisture contents.

Table 2 Test scheme

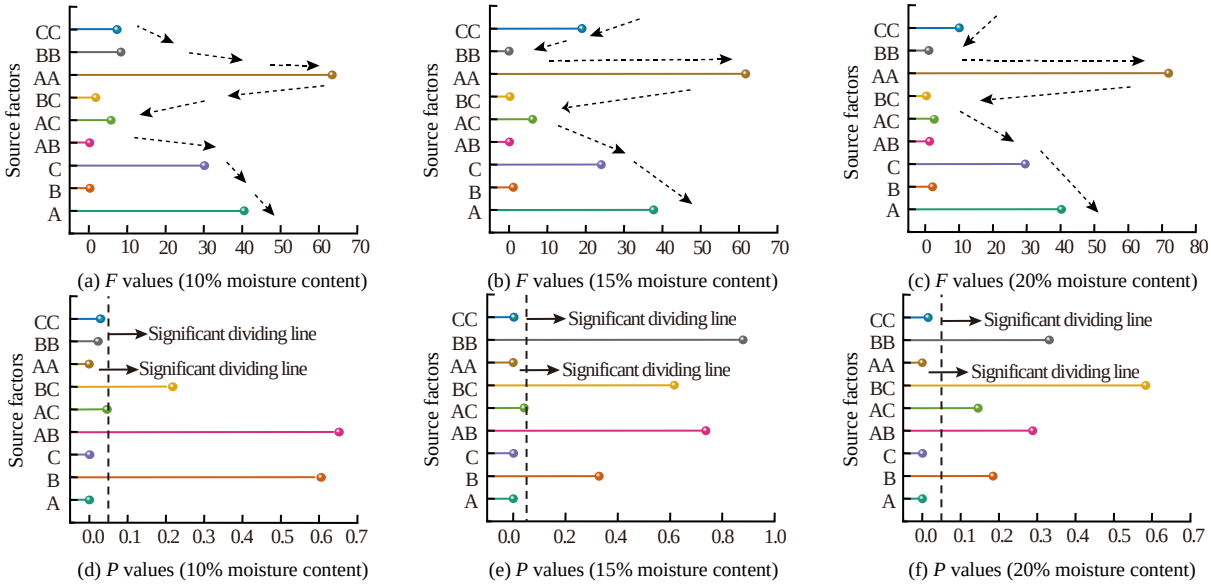
No.	Factor A%	Factor B%	Factor C%	No.	Factor A%	Factor B%	Factor C%
1	30	12	18	10	36	6	18
2	42	0	18	11	36	0	12
3	36	6	18	12	36	0	24
4	36	6	18	13	30	0	18
5	42	6	12	14	36	12	12
6	30	6	24	15	36	6	18
7	42	12	18	16	42	6	24
8	36	6	18	17	30	6	12
9	36	12	24	—	—	—	—



(a) Different model *F* values (b) Different model *P* values (c) Different model C_V values (d) Different model R^2 values

Fig.5 Fitted data of different models

As illustrated in Fig. 6, the analysis of variance for the matric suction fitting model of the sample indicates that factors A and C are significant, whereas factor B is not. The significance level of factor A exceeds that of factor C, resulting in a hierarchy of significance as follows: A > C > B. The matric suction values at 10%, 15%, and 20% moisture content are influenced not only by individual factors but also by the interactions between factors, specifically the AC and AB interactions, which are significant. In contrast, the interactions between AB and BC are not significant. Given that the magnitude of the *F*-value reflects the influence of various factors on the sample's matric suction, a larger F-value signifies a greater impact[32]. Consequently, under this model, both factors A and C exert substantial influence on the results, with the degree of influence being A > C > B. In summary, kaolinite powder exerts the most significant influence on the matric suction of samples with moisture contents of 10%, 15%, and 20%, followed by illite powder and montmorillonite powder.



(a) *F* values (10% moisture content) (b) *F* values (15% moisture content) (c) *F* values (20% moisture content)

(d) *P* values (10% moisture content) (e) *P* values (15% moisture content) (f) *P* values (20% moisture content)

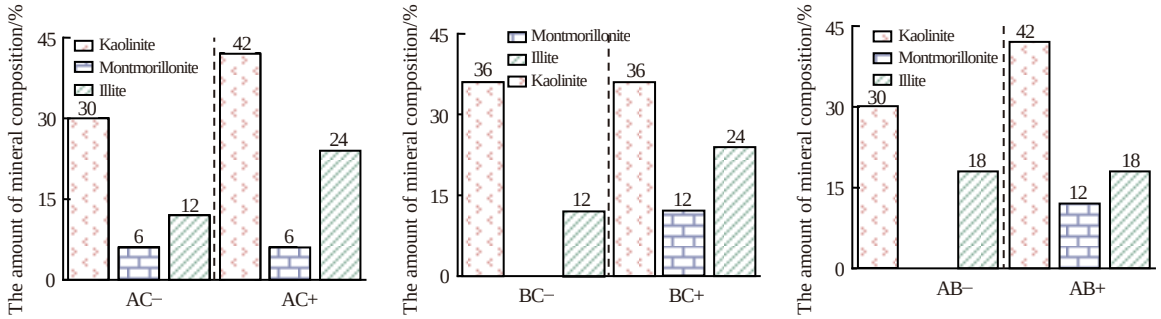
Fig.6 Analysis of variance of different models

3.2 Analysis of soil-water characteristic curve

According to the response surface analysis, the matric suction of red soil is influenced by the interaction among kaolinite powder (factor A), montmorillonite powder (factor B), and illite powder (factor C). Therefore, a series of experiments was designed to test the matrix

suction at the highest and lowest values for each pair of additives (denoted as AC+, AC−; AB+, AB−; BC+, BC−). The specific content of the three mineral components is illustrated in Fig.7.

The soil-water characteristic curves (SWCCs) of the six sample groups were fitted using the GA model, VG model, FX model, and the three-parameter VG model. The fitting equations are presented in Eq.（4）−（7）, and the fitting parameters are summarized in Table 3. Based on the fitting parameters and Fig.8, it can be observed that the four fitting models exhibit similar curve performance in the near-saturation and transition regions, while significant differences are noted in the residual region. All models provide satisfactory fitting results with correlation coefficients exceeding 0.95. After comprehensive analysis and comparison, the VG model demonstrates the best fitting performance, and thus it was selected for parameter fitting in this study.



(a) Dosage of AC group (b) Dosage of BC group (c) Dosage of AB group

Fig.7 Mineral composition content

Table 3 Parameter fitting for various samples

Source factors	GA model				VG model				FX model				Three-parameter VG model			
	a	*n*	*m*	R^2	*a*	*n*	*m*	R^2	*a*	*n*	*m*	R^2	*a*	*n*	*m*	R^2
AC+	2.79	6.11	—	0.976	2.69	6.50	—	0.983	2.69	6.28	2.10	0.979	0.38	6.25	0.77	0.978
AC−	2.74	4.95	—	0.982	2.58	5.26	—	0.999	2.49	5.02	1.78	0.995	0.41	5.13	0.68	0.998
BC+	2.97	4.88	—	0.998	2.79	5.39	—	0.999	2.79	4.50	4.30	0.996	0.26	4.50	2.48	0.974
BC-	3.13	6.17	—	0.979	2.98	6.18	—	0.998	2.98	5.99	2.04	0.997	0.35	5.72	0.64	0.977
AB+	2.95	5.36	—	0.953	2.80	5.58	—	0.999	2.69	5.20	1.73	0.990	0.36	5.05	0.75	0.998
AB−	2.76	4.92	—	0.985	2.60	5.23	—	0.999	2.50	5.01	1.76	0.995	0.40	4.86	0.74	0.997

Figure 8 illustrates the soil-water characteristic curves of compacted samples with varying mineral compositions. During the evolution of the humidification process, the soil-water characteristic curve can be distinctly categorized into three characteristic regions based on the quantitative threshold of substrate suction force. Specifically, when the substrate suction force is less than 100 kPa, it corresponds to the near-saturation region; the range from 100 kPa to 10 000 kPa represents the transition region, and the range exceeding 10 000 kPa pertains to the residual region. In summary, the soil-water characteristic curves derived from the experiments can be systematically classified into three stages: the near-saturation stage, the transition stage, and the residual stage. In the near-saturation region, where pores are predominantly filled with water and samples approach full saturation, the variation in suction is relatively limited. Consequently, the influence of different mineral components on this region is minimal, and the curves for all samples exhibit similar characteristics. As suction increases, the sample transitions into the transition region. Here, the curve's slope becomes significantly steeper, indicating an accelerated rate of water loss and a gradual decrease in saturation. At this stage, the impact of mineral composition on the curve's slope becomes apparent. Specifically, samples with higher kaolinite content exhibit a steeper slope and a more pronounced reduction in water content as suction increases. Conversely, samples rich in montmorillonite and illite display a gentler slope, resulting in a broader range of suction changes. Upon entering the residual region, the remaining water content is minimal, and further increases in matrix suction induce only minor variations in water content. As such, the curves for all samples flatten out in this region. Through the graphical method, the intake air value (AOV) and residual value for each group of samples were determined. The detailed operational steps are as follows: First, on the soil-water characteristic curve, identify the suction value corresponding to the point where the curve's slope begins to increase significantly; this value represents the intake air value (AOV). Subsequently, in the residual region, determine the moisture content value corresponding to the point where the curve tends to plateau; this value represents the residual value. When all three mineral components are present in high concentrations, the AOV of the AC+ group is notably higher than that of the other two groups. Additionally, the AOV and residual values of the AC+ and AB+ groups exceed those of the AC− and AB− groups, while the AOV and residual values of the BC+ group are considerably lower than those of the BC− group, with the residual values showing an inverse relationship.

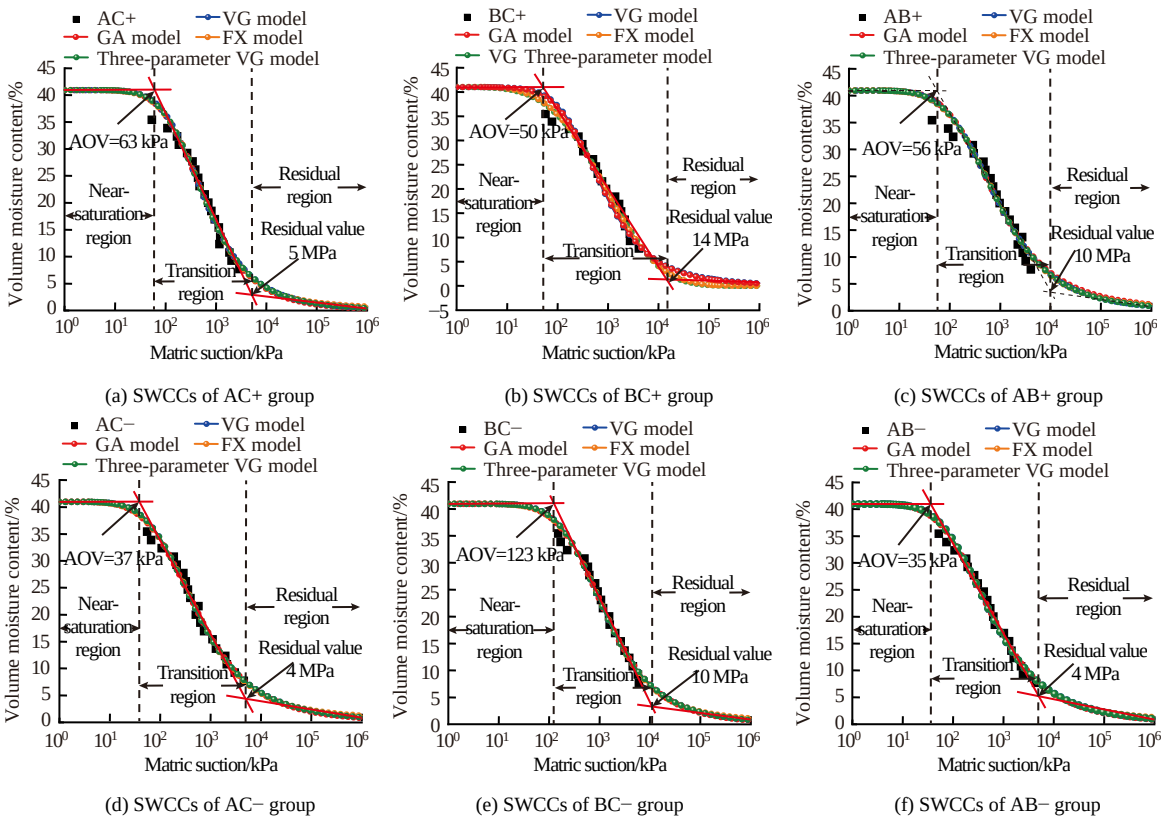


Fig.8 Soil-water characteristic curves of compacted samples with different mineral compositions

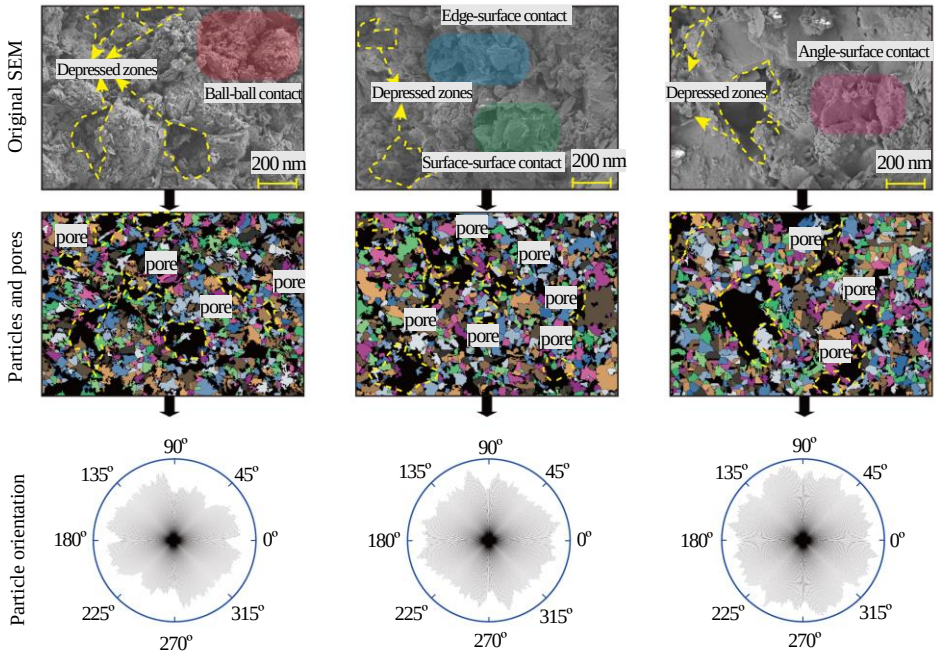
3.3 Characteristics of pore structure and pore distribution

Among the six groups of soil-water characteristic curve test samples, three combinations (AC+, AB+, BC+) with the highest pairwise component content were selected for scanning electron microscope (SEM) analysis. Their microstructures are illustrated in Fig.9. In samples with higher kaolinite and illite contents (see Fig. 9(a)), upon hydration, the fine clay particles exhibit hydrophilic behavior, absorbing water and expanding, thereby becoming more viscous. Due to the high concentration of both minerals, a significant number of clay particles adhere to the surface of sand grains through physical adsorption and chemical bonding. This process forms a dense coating layer on the sand grain surfaces, rendering their original boundaries irregular and promoting the formation of flocculated structures. These flocculated structures are voluminous and interwoven, leading to the development of macroporous structures within the sample. Within this structure, the predominant particle contact mode is ball-to-ball contact. Conversely, when the kaolinite and montmorillonite contents are substantial (see Fig. 9(b)), the interaction between kaolinite particles is relatively weak, and the montmorillonite content is insufficient to form extensive flocculated connections. As a result, fewer aggregated flocculated structures are observed in the sample. The sand grain boundaries remain relatively smooth, with some fine clay particles filling the pores, forming a relatively loose dispersed structure. By contrast, in samples with elevated montmorillonite and illite contents (see Fig. 9(c)), no prominent flocculated structure is evident. Instead, a large number of clay particles are tightly packed within the pores, forming a dispersed structure characterized by tighter arrangements and smaller pore diameters. Here, the particle contact modes shift to surface-to-surface and angle-to-edge contacts.

The pore volume accumulation and density distribution curve of compacted soil samples, as measured by the mercury injection test, are collectively referred to as the pore size distribution curve (PSDC). This is commonly represented as the cumulative pore volume and size distribution curve[33]. Using the mercury injection test, the porosity and pore distribution curves for compacted samples with varying mineral compositions are presented in Figs.10 and 11. In samples with higher montmorillonite and illite content, the porosity, total pore area, and total pore volume are relatively high, while the average pore diameter is comparatively small. Conversely, the combination of high kaolinite and illite contents exhibits the largest average pore diameter among the three types (Fig.10). These findings from the porosity analysis align with observations made using scanning electron microscopy.

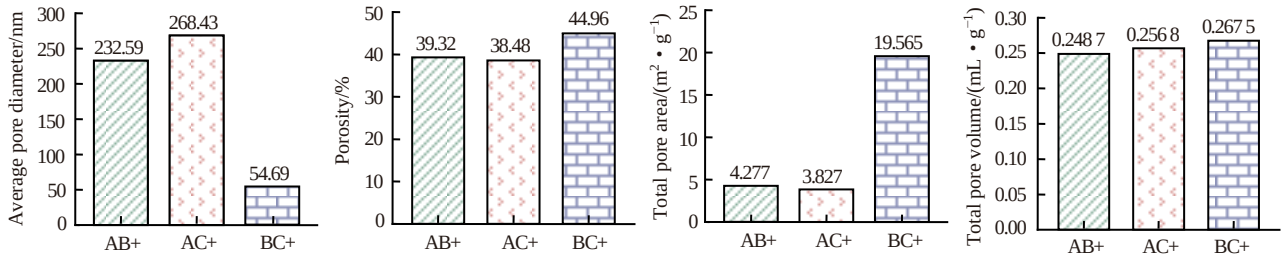
By analyzing the pore distribution curves, it is evident that the cumulative mercury intrusion volume and area exhibit a unimodal pattern (see Fig.11(a), 11(c), and 11(e)). Specifically, the cumulative mercury intrusion volume curve demonstrates an initial rapid increase followed by a gradual decrease, whereas the mercury intrusion area curve shows the opposite trend. The peak values of both curves occur within the micropore and small pore ranges, indicating that these pore

sizes dominate the sample. In contrast, the incremental mercury intrusion volume of the sample displays a bimodal pattern (see Fig.11(b), 11(d)). The minor peaks correspond to intragranular pores form by clay particles, while the major peaks represent intergranular pores between skeletal particles. Both peaks fall within the mesopore range, and the presence of low valleys suggests significant variations in pore size and distribution. Additionally, the peak point in the pore volume increment distribution curve for samples with higher kaolinite and illite contents is relatively higher due to their larger pore volumes. The logarithmic difference mercury intake curves of different samples show obvious peaks in the mesopore range (see Fig.11(f)), indicating that the mesopore is the main contribution pore size range for mercury intake, which echoes the bimodal characteristics of the incremental mercury intake volume and further confirms the important position of the mesopore in the pore structure. The sample with the highest content of kaolinite and illite has a relatively higher peak value of mercury intake in logarithmic difference. Combined with the previous analysis of pore volume, this is because the pore volume of this sample is large, and the rate of change of mercury intake in key pore size intervals such as mesopoids is also greater, indicating that its pore structure is more "active" during the mercury intake process. It also reflects the significant influence of different mineral compositions on pore structure and mercury intrusion behavior.



(a) AC+ (b) AB+ (c) BC+

Fig.9 Microstructural analysis of compacted samples with varied mineral compositions



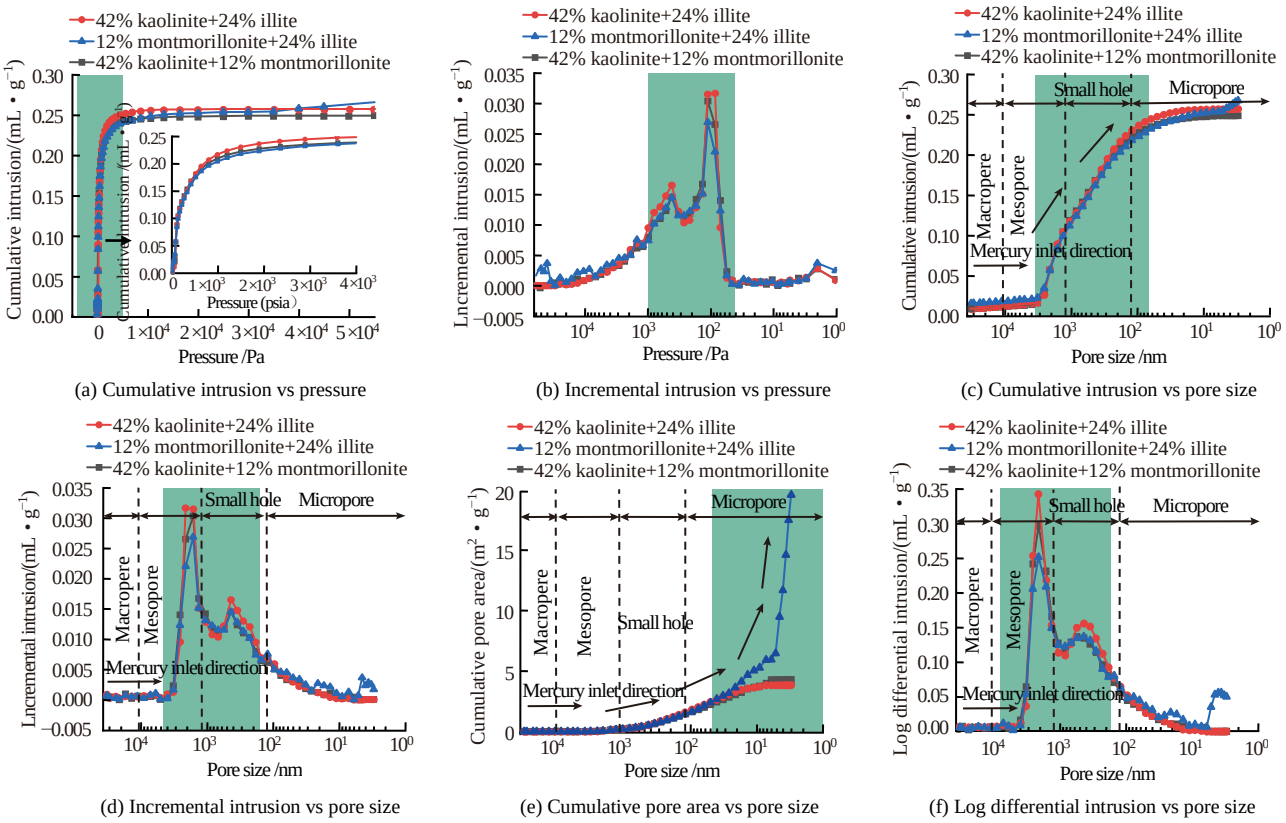
(a) Average pore size of different samples (b) The porosity of different samples (c) Total pore area of different samples (d) Total pore volume of different samples

Fig.10 Porosities of compacted samples with different mineral compositions

3.4 Pore structure characteristic parameters

In order to quantitatively analyze the pore structure characteristics of the three samples, images acquired via scanning electron microscopy (as depicted in Fig.9) were utilized in conjunction with the PCAS image analysis software for detailed processing. Using this software, several key parameters characterizing the pore structures of the three sample groups were successfully extracted, including average area, average perimeter, porosity, fractal dimension, and probability entropy. The specific results are presented in Fig.12. Among the samples, those in the AC+ group exhibited characteristics of large pore sizes but relatively low porosity. This could potentially be attributed to the relatively loose flocculent structure formed by clay minerals within the AC+ group samples. Despite the presence of larger individual pores, the poor connectivity between these pores led to a lower overall porosity.

Conversely, the samples in the BC+ group demonstrated an opposite trend (as shown in Figs. 8(c)−8(e)). This may have resulted from the close packing of viscous particles within the pores of the BC+ group samples. Although the pore sizes were smaller, the higher number of pores contributed to a relatively greater overall porosity. Additionally, the AC+ group had a smaller average shape factor, indicating smoother particle morphology. Simultaneously, its average circumference was the largest, suggesting relatively longer particle boundaries (see Fig.12(b)). These findings align with the descriptions provided in Section 3.3.



(a) Cumulative intrusion vs pressure (b) Incremental intrusion vs pressure (c) Cumulative intrusion vs pore size

(d) Incremental intrusion vs pore size (e) Cumulative pore area vs pore size (f) Log differential intrusion vs pore size

Fig.11 Pore distribution curves of compacted samples with different mineral compositions

The area probability distribution index of the three sample groups exhibited a certain correlation with the average area (see Fig.12(a)). Specifically, the AC+ group demonstrated the lowest area probability distribution index, which corresponded to a relatively smaller average area, whereas the BC+ group displayed an opposite trend. This suggests that a higher area probability distribution index is associated with greater heterogeneity in the particle or pore area distribution within the soil, potentially leading to a higher proportion of large-area particles or pores and consequently increasing the average area. Additionally, it is noteworthy that the AC+ group exhibits a larger fractal dimension but a relatively smaller probabilistic entropy (see Fig.12(f), 12(i)). This phenomenon can primarily be attributed to the flocculent structure formed by the AC+ group particles, where individual particle surfaces are smooth, yet the overall distribution of particles and pores remains highly irregular and complex. Despite this complexity, the spatial arrangement of these particles and pores maintains a certain degree of order. This characteristic aligns with the results of the ordering coefficient, consistency coefficient, curvature coefficient, and porosity fractal dimension of the samples (see Fig.12(g), 12(h)), further validating the unique pore structure features of the AC+ group samples.

4 Discussion

4.1 Influence of interaction of two factors on matrix suction

The test data were systematically analyzed and organized. Based on the actual recorded data and the fitted regression equation, a correlation diagram was constructed to illustrate the relationship between the residuals and the predicted values of the equation, as depicted in Figs.13(a)–13(c). As evident from the figures, the scatter distribution of residuals versus predicted values exhibits an irregular pattern. The color points representing the values are randomly distributed within a specific interval without any discernible trend or pattern. This indicates that the regression model maintains consistent error distribution characteristics across different predicted values, thereby further enhancing the robustness and reliability of the model. Additionally, using the regression model, the influence of the interaction between two factors on the matric suction of red soil was investigated.

When the content of illite powder (factor C) is fixed at 18%, the contour plots illustrating the interaction between kaolinite-montmorillonite powder and matrix suction are

presented in Figs.13(d)–13(f). As observed from these figures, an overall upward trend in matrix suction is evident with increasing kaolinite powder content. Although montmorillonite powder content has some influence, this effect is not pronounced. The matrix suction reaches its peak when the kaolinite powder content is approximately 36% and the montmorillonite powder content is around 6%. As the water content of the sample increases, the contours become more concentrated, and the midline area gradually assumes an elliptical shape, indicating that the interaction between kaolinite and montmorillonite powders becomes increasingly significant. This suggests that the interaction has the greatest impact on samples with 20% water content and the least impact on those with 10% water content. When the content of montmorillonite powder (factor B) is fixed at 6%, the contour diagrams depicting the interaction between kaolinite-illite powder and matrix suction are shown in Figs.13(g)−13(i). With a constant montmorillonite powder content, matrix suction increases as the kaolinite and illite powder contents rise. Notably, the curve for kaolinite powder is steeper than that for illite powder, indicating a more substantial effect of kaolinite powder on matrix suction. The matrix suction peaks when the kaolinite powder content is approximately 36% and the illite powder content is around 18%. The contours are relatively dense, and the central region forms an ellipse, signifying a relatively significant interaction between the two factors. As water content increases, the curvature of the ellipse also increases, suggesting a greater influence on samples with 20% water content and the least influence on those with 10% water content.

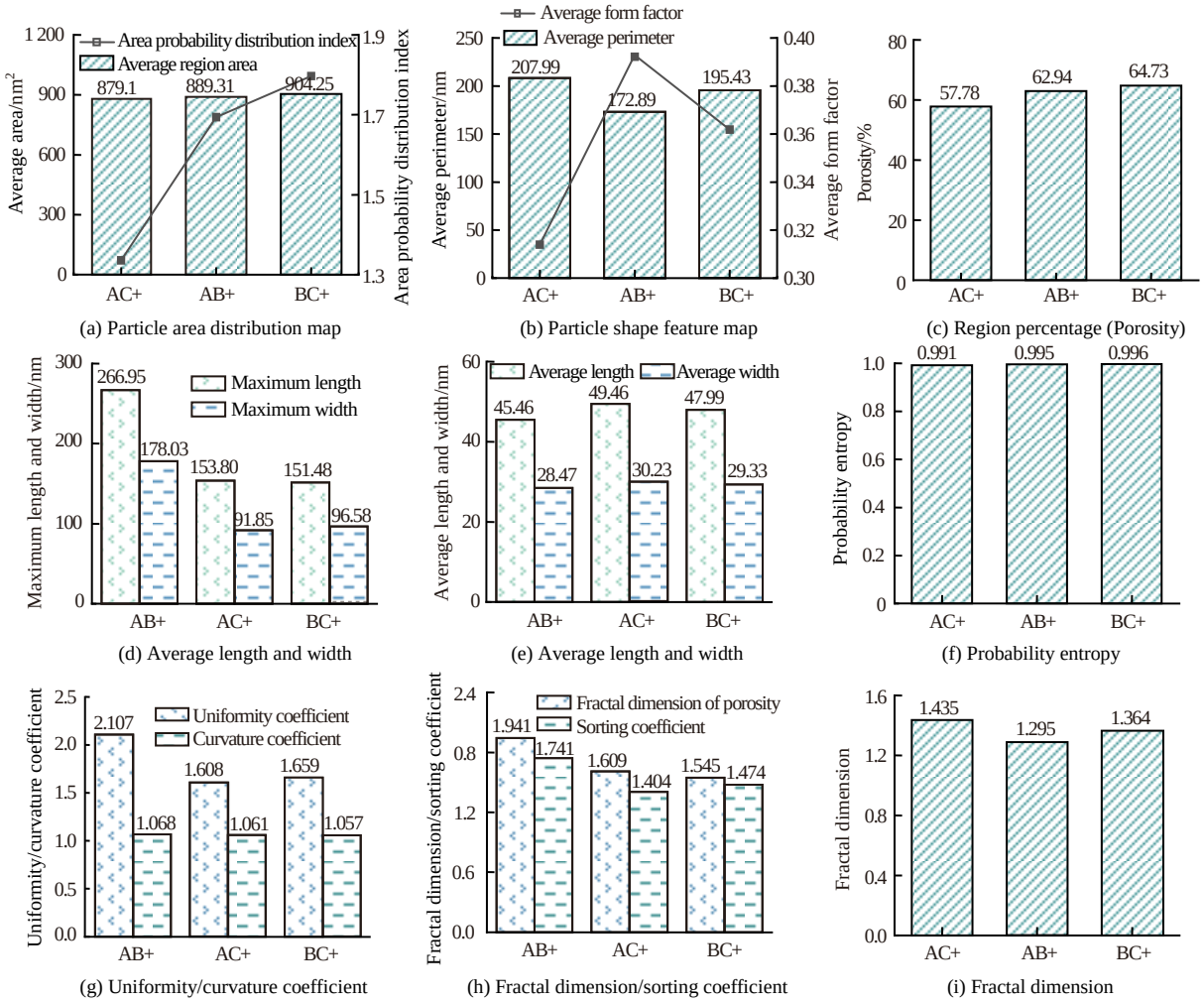


Fig.12 Pore characteristic parameters of compacted samples with different mineral compositions

Longitudinal comparison reveals that, under identical sample water content conditions, the influence of kaolinite-illite powder on matrix suction is significantly greater than that of kaolinite-montmorillonite powder. The results of response surface analysis align with the variance analysis depicted in Fig.6, allowing for mutual validation between the two methods. This phenomenon can be attributed to the fact that, despite montmorillonite's strong hydrophilic properties and its non-negligible contribution to matrix suction, its relative abundance in the mixture is comparatively low[34]. Consequently, while the interaction between kaolinite and montmorillonite does exert some influence on matrix suction, this effect is considerably weaker compared to that of kaolinite-illite powder.

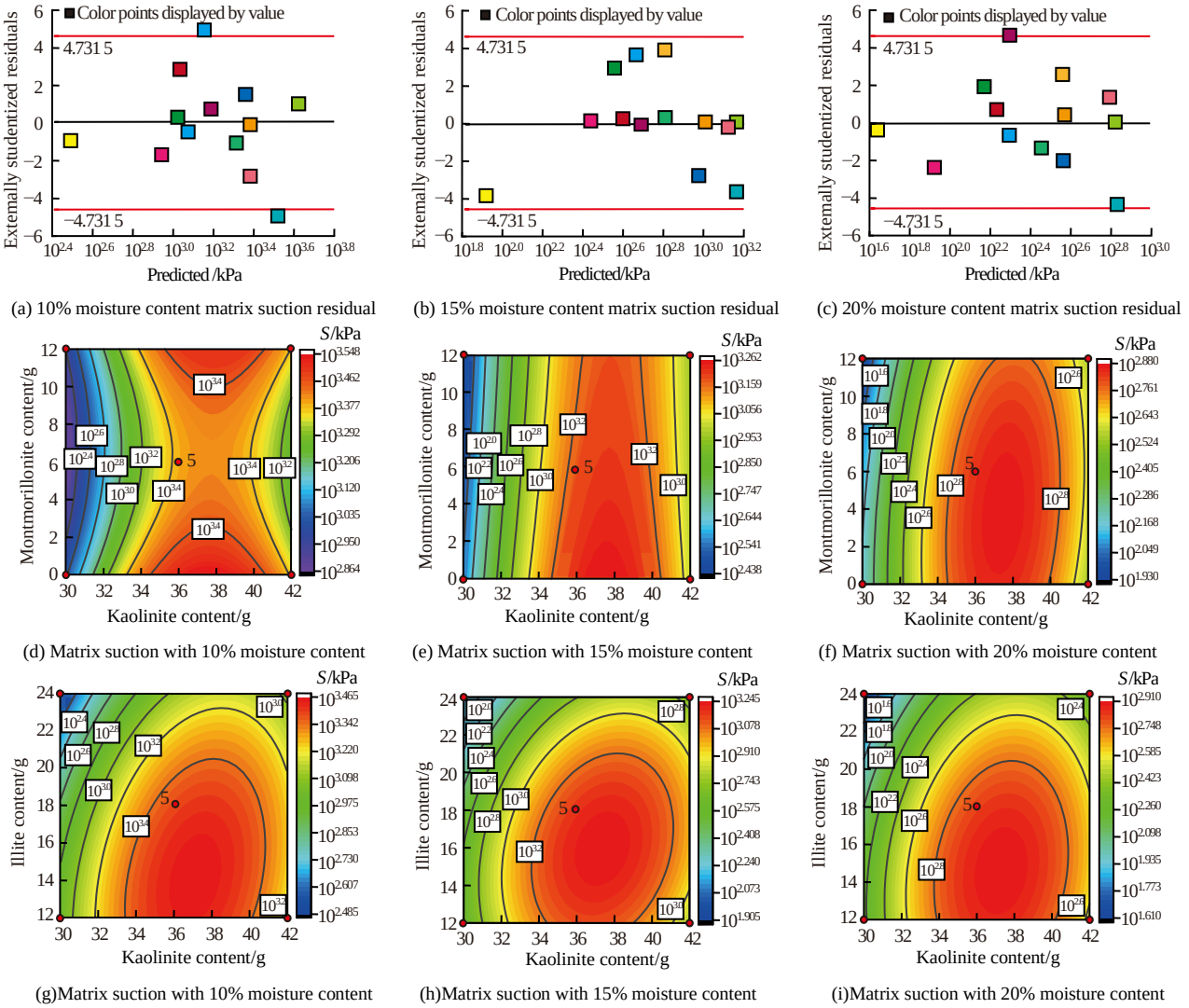
4.2 Effect of microstructure on soil-water characteristic curve

The Young-Laplace equation correlates the pore size of

soil with matric suction, thereby bridging the micro-pore structure of soil to its macroscopic soil-water characteristics. This relationship is expressed as follows:

$$\varphi = u_a - u_w = \frac{4T_s \cos \partial}{D} \quad (8)$$

where u_a is the pore gas pressure (kPa); u_w is the pore water pressure (kPa); the difference between the two, u_a–u_w, represents matrix suction; T_s is the surface tension of water (At 20 ℃, the value of 0.727 N m^{-1} is adopted); ∂ represents the contact angle between soil particles and water, which is generally assumed to be 0; and D denotes the pore diameter in nanometers (nm).



(a) 10% moisture content matrix suction residual (b) 15% moisture content matrix suction residual (c) 20% moisture content matrix suction residual

(d) Matrix suction with 10% moisture content (e) Matrix suction with 15% moisture content (f) Matrix suction with 20% moisture content

(g)Matrix suction with 10% moisture content (h)Matrix suction with 15% moisture content (i)Matrix suction with 20% moisture content

Fig.13 Residual matric suction and contours of interaction effects between two factors on the matric suction of red soil

The horizontal aperture data obtained from the mercury injection test were converted into matrix suction values using Eq.（8）. Subsequently, the influence of pore size distribution curves (PSDC) on soil-water characteristic curves (SWCC) was analyzed and correlated, as illustrated in Fig.14.

As evident from the figure, there is a strong correlation between SWCC and PSDC curves. In the three compacted soil samples with varying mineral compositions, pores with dominant sizes serve as the primary water storage spaces. The quantity and range of these pores significantly affect the sample's water content, with even minor changes causing substantial fluctuations. Consequently, the dominant aperture range in the PSDC aligns well with the transition region of the SWCC. When the pore diameter distribution density is high, the number of pores is large and concentrated within this range, leading to a steep slope in the soil-water characteristic curve. Conversely, when the pore diameter distribution density is low, the slope becomes relatively gentle. Due to the limited water storage capacity associated with low pore diameter distribution density, variations in pore number and range have minimal impact on soil water content, resulting in a more gradual trend in the soil-water characteristic curve. Analysis and comparison of the three samples with different mineral compositions reveal that those with higher kaolinite and illite contents exhibit larger predominant pore sizes and steeper slopes in the transition zone. This is primarily attributed to the dominant role of capillary action in this region, which influences water distribution and flow. Increased kaolinite and illite contents lead to larger pore sizes, thereby weakening capillary action to some extent. Additionally, the

other two groups of samples have smaller pore sizes, enhancing capillary effects within the soil, improving water retention capacity, and resulting in a relatively gentle slope in the soil-water characteristic curve. In conjunction with the pore microstructure characteristics illustrated in Fig.9, it is evident that samples containing higher proportions of kaolinite and illite exhibit a relatively larger pore structure due to the formation of flocculated structures within. Results in an increased number of flow channels for water, thereby enhancing soil permeability. However, the presence of larger pores also diminishes the soil's water retention capacity, leading to a steeper slope in the transition section of the soil-water characteristic curve. Conversely, the other two sample groups display a dispersed and tightly arranged pore structure with smaller pore diameters, which restricts water flow and significantly intensifies the capillary effect, thus resulting in a more gradual slope in the transition region of the soil-water characteristic curve.

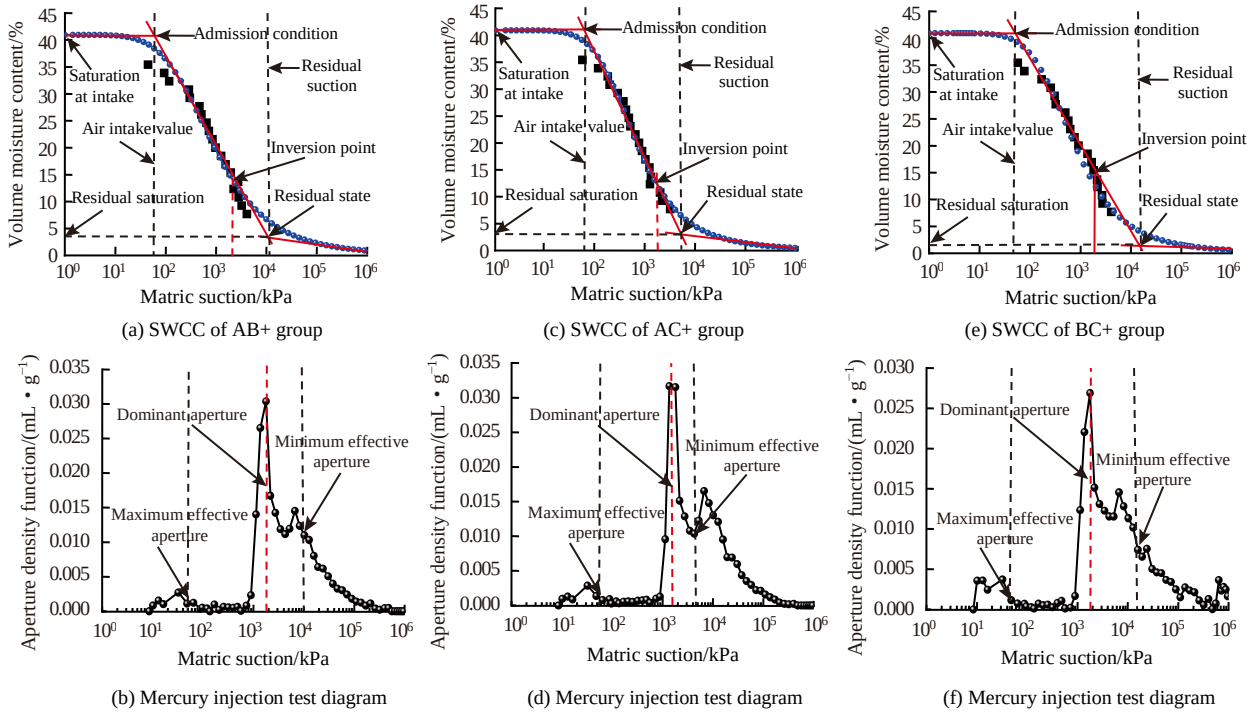


Fig.14 Corresponding relationship between pore distribution in compacted samples with varying mineral compositions and soil-water characteristic curves

4.3 Effect of mineral composition on microscopic mechanism of red soil

The microscopic mechanism of red soil is significantly influenced by the hydrophilic and hydrophobic characteristics of its mineral composition, as illustrated in Fig.15. These properties are typically associated with the surface structure and chemical composition of the minerals. Montmorillonite, for instance, has a surface enriched with polar hydroxyl groups (−OH). Upon contact with water, these hydroxyl groups dissociate or ionize, releasing hydrogen ions or radicals that form hydrogen bonds with oxygen atoms in adjacent water molecules. Simultaneously, negatively charged oxygen ions or hydroxyl radicals interact with hydrogen atoms in water molecules, forming extensive hydrogen-bond networks. This strong interaction enhances the adsorption and retention of water molecules on the mineral surface. Furthermore, the high degree of hydroxyl dissociation on montmorillonite surfaces facilitates numerous hydrogen bonds with water molecules, contributing to its pronounced hydrophilicity (see Figs. 15(b), 15(c)). Additionally, the rough surface texture reduces surface energy, promoting water molecule spreading and adsorption (see Fig.15(d)). Conversely, hydrophobic minerals such as kaolinite exhibit opposing characteristics (see Figs. 15(f), 15(g)). Moreover, van der Waals forces universally act as weak intermolecular forces between both hydrophilic and hydrophobic mineral surfaces and water molecules, enhancing water molecule adsorption and infiltration (see Fig.15(e)). Hydrolysis and ion exchange reactions also occur among mineral components. Hydrolysis reactions transform kaolinite into kaolinite-hydrate upon water contact, increasing layer spacing and influencing pore connectivity and size. Ion exchange reactions alter the surface charge distribution and interlayer structure of illite, such as the replacement of K^+, Ca^{2+}, and Na^+ with dissolved Fe^{3+}, thereby affecting pore morphology and stability (see Fig.15(h)).

The disparity in mineral hydrophilicity serves as the central mechanism governing the microstructural evolution of red soil. The hydroxyl-containing functional groups within kaolinite exhibit moderate hydrophilicity, which results in controlled hydration expansion and an interlayer domain structure that restrains excessive swelling. In contrast, the permanent negative charges generated by lattice substitution in montmorillonite possess strong hydrophilic properties, leading to a marked increase in particle spacing. Moreover, the synergistic interaction between mineral surface

characteristics and chemical reactions dictates the mode of particle connectivity. The smooth basal surface structure of kaolinite restricts mechanical interlocking, while weak chemical bonds between minerals struggle to sustain stable connections. Although montmorillonite can facilitate the formation of micro-aggregates through its high charge density, it fails to construct an effective flocculent network framework when present in insufficient quantities. In the combined system of these two minerals, the water film lubrication effect induced by strongly hydrophilic minerals and the reduced frictional resistance due to the smooth surface mutually reinforce each other, substantially diminishing particle connection strength and ultimately driving the soil's evolution toward a loose and dispersed structure.

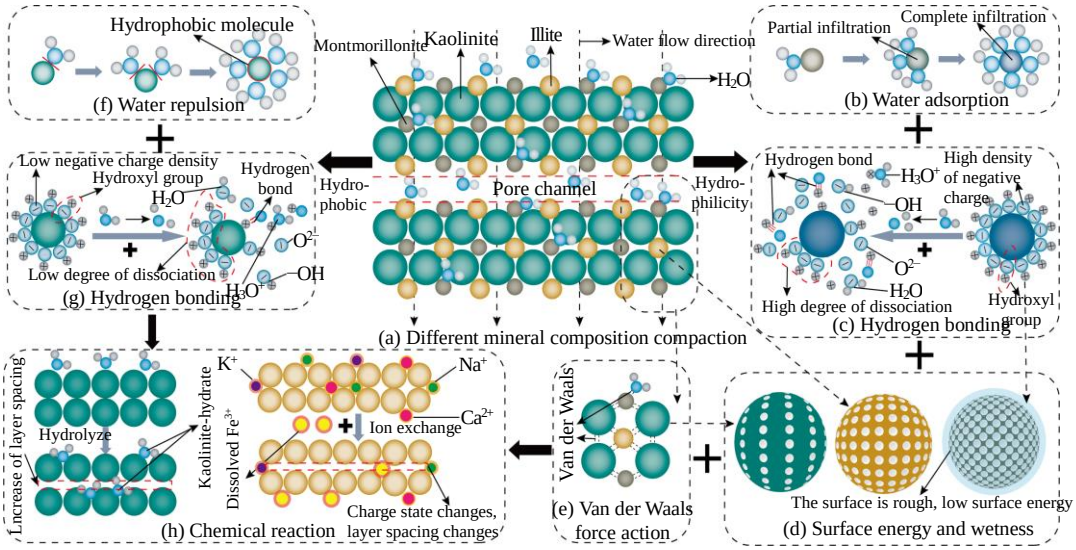


Fig.15 Influence of varied mineral compositions on the micromechanical properties of red soil

5 Conclusions

In this paper, the impact of mineral composition ratios on matrix suction of red soil is systematically examined using the response curve method. Laboratory experiments yielded soil-water characteristic curves, microscopic plane images, and pore distribution curves for key proportions. Comparative analysis of these results led to the following conclusions:

(1) The quadratic polynomial regression model, designed and constructed based on the Box-Behnken methodology, successfully quantified the nonlinear relationship between the contents of kaolinite, montmorillonite, and illite and the matrix suction under moisture content conditions of 10%, 15%, and 20%. Analysis of variance revealed that the content of kaolinite was the predominant factor influencing matrix suction, followed by illite, with montmorillonite having the least impact.

(2) The analysis of the interaction between the two factors reveals that moisture content exerts a regulatory influence on mineral interaction effects. Specifically, under conditions of high moisture content (20%), the interaction effects of kaolinite with montmorillonite and illite on matrix suction are significantly enhanced. Notably, the impact of the kaolinite-illite interaction is considerably greater than that of the kaolinite-montmorillonite interaction.

(3) The influence of mineral composition on the soil-water characteristic curve exhibits regional specificity. In the transition zone, samples predominantly composed of kaolinite display a steeply rising curve characteristic, whereas samples dominated by montmorillonite or illite exhibit a gentle curve. When kaolinite and illite coexist, the air intake value of the sample is significantly higher compared to other combinations, suggesting that this mineral combination can substantially enhance the water retention capacity of the soil.

(4) Microstructural characterization reveals that the kaolinite-illite composite system forms a multi-level pore network predominantly consisting of large pores through the promotion of flocculent structure development. The probability distribution index of the pore area exhibits a negative correlation with the average pore diameter. This pore characteristic is in complete correspondence with the range of the transition zone in the soil-water characteristic curve, thereby elucidating the mineralogical dependence of macroscopic hydraulic properties at the microscopic scale.

Data availability statement

The author confirms that the data supporting the findings of this study are available within the article.

Declaration of competing interest

All authors certify that they have no affiliations with or involvement in any organization or entity with any financial interest or non-financial interest in the subject matter or materials discussed in this manuscript.

References

[1] LIU H S, RAHARDJO H, SATYANAGA A. Use of osmotic tensiometers in the determination of soil-water characteristic curves[J]. **Engineering Geology**, 2023, 312: 106938.

[2] PENG J P, HU H, ZHANG J. Rapid testing and prediction of soil-water characteristic curve of subgrade soils considering stress state and degree of compaction[J]. **Journal of Rock Mechanics and Geotechnical Engineering**, 2023, 15(12):

3305−3315.

[3] LIU Q X, TANG L S, CHEN Y. Response of soil-water characteristics to pore structure of granite residual soils[J]. **Soils and Foundations**, 2023, 63(6): 101395.

[4] GUO Z Q, LIU L F, TANG T. Influence of leaching solution on the soil-water characteristics of ion-absorbed rare earth minerals and its hysteresis effect[J]. **Minerals**, 2023, 13(5): 637.

[5] YAN W, BIRLE E, CUDMANI R. A new framework to determine general multimodal soil water characteristic curves[J]. **Acta Geotechnica**, 2021, 16(10): 3187−3208.

[6] LI Y, ALVES R, VANAPALLI S. Models for considering the thermo-hydro-mechanical-chemo effects on soil- water characteristic curves[J]. **Geosciences**, 2024, 14(2): 38.

[7] MALAYA C, SREDEEP S. Critical review on the parameters influencing soil-water characteristic curve[J]. **Journal of Irrigation and Drainage Engineering**, 2012, 138(1): 55−62.

[8] TANG Xiao-lin, TONG Li-hong, XU Chang-jie, et al. Model for soil-water characteristic curve considering grain-size distribution and deformation of soils[J]. **Chinese Journal of Geotechnical Engineering**, 2025, 47(8): 1629−1640.

[9] FU Ying-peng, LIAO Hong-jian, LÜ Long-long, et al. Hysteretic model for fitting soil-water characteristic curves considering contact angle and grain-size distribution[J]. **Chinese Journal of Geotechnical Engineering**, 2022, 44(3): 502−513.

[10] WANG X Q, ZHANG X C, PEI X J, et al. Effect of the particle size composition and dry density on the water retention characteristics of remolded loess[J]. **Minerals**, 2022, 12(6): 698.

[11] LU Xing-zhi, LIU Xiao-wen, CHEN Ming, et al. Soil-water characteristic curve based on particle contact model using three unequal particle sizes[J]. **Rock and Soil Mechanics**, 2018, 39(2): 651−656.

[12] SUN Yin-lei, TANG Lian-sheng, LIU Jie. Advances in research on microstructure and intergranular suction of unsaturated soils[J]. **Rock and Soil Mechanics**, 2020, 41(4): 1122−1905.

[13] CHEN X R, MA M L, ZHOU S M, et al. Effect of initial conditions on the pore structure and bimodal soil-water characteristic curve of compacted granite residual soil[J]. **Processes**, 2024, 12(2): 409.

[14] LI L C, LI X A, LI Y, et al. Assessing the relationships among the initial conditions, PSD and SWCC of compacted soil[J]. **Scientific Reports**, 2025, 15(1): 10327.

[15] WANG Yu, LI Tong-lu, LEI Yu-lu, et al. Responding of soil-water characteristics of compacted loess soil to its pore structure[J]. **Chinese Journal of Rock Mechanics and Engineering**, 2022, 41(6): 1246−1255.

[16] ZHANG Yu-wei, SONG Zhan-ping, XIE Yong-li. Prediction model for soil-water characteristic curve of loess under porosity change[J]. **Chinese Journal of Geotechnical Engineering**, 2022, 44(11): 2017−2025.

[17] ZHAO Y, RAHARDJO H, SATYANAGA A. A general best-fitting equation for the multimodal soil–water characteristic curve[J]. **Geotechnical and Geological Engineering**, 2023, 41(5): 3239−3252.

[18] WANG Shi-ji, WANG Xiao-qi, LI Da, et al. Evolution of fissures and bivariate-bimodal soil-water characteristic curves of expansive soil under drying-wetting cycles[J]. **Chinese Journal of Geotechnical Engineering**, 2021, 43(Suppl. 1): 58−63.

[19] CUI Hong-huan, QIN Xiao-peng, WANG Wen-tao, et al. Effect of freeze-thaw cycle on SWCC and strength of unsaturated silty clay[J]. **Chinese Journal of Underground Space and Engineering**, 2020, 16(6): 1722−1728, 1745.

[20] LUO Qi-xun, HUANG Jin, CHEN Qun. Influence of vertical stress and dry density on soil-water characteristic curve of gravelly soil[J]. **Rock and Soil Mechanics**, 2014, 35(3): 729−734, 743.

[21] CHEN Q, SU W, WANG H. Vertical stress effects on soil-water characteristics of fly ash[J]. **Soil Mechanics and Foundation Engineering**, 2022, 59(3): 265−271.

[22] PHAM T A, SUTMAN M. Modeling the combined effect of initial density and temperature on the soil-water characteristic curve of unsaturated soils[J]. **Acta Geotechnica**, 2023, 18(12): 6427−6455.

[23] PHAM T A, HASHEMI A, SUTMAN M. Effect of temperature on the soil-water retention characteristics in unsaturated soils: analytical and experimental approaches[J]. **Soils and Foundations**, 2023, 63(3): 101301.

[24] WANG Zhao, YANG Jin-xin, KUANG Juan-juan, et al. Application of filter paper method in field measurement of matric suction[J]. **Chinese Journal of Geotechnical Engineering**, 2003, 25(4): 405−408.

[25] MATLLAN S J, TAHA M R, MUKHLISIN M. Assessment of model consistency for determination of soil-water characteristic curves[J]. **Arabian Journal for Science and Engineering**, 2016, 41(4): 1233−1240.

[26] YANG W, CLIFFORD D, MINASNY B. Mapping soil water retention curves via spatial Bayesian hierarchical models[J]. **Journal of Hydrology**, 2015, 524: 768−779.

[27] WANG S J, LI W W, CHEN Z Y, et al. Effect of C_r on the performance of Fredlund and Xing (1994)'s equation in best fitting soil-water characteristic curve data[J]. **Results in Engineering**, 2022, 13: 100373.

[28] PRAKASH A, HAZRA B, SEKHARAN S. Probabilistic analysis of soil-water characteristic curve of bentonite: multivariate copula approach[J]. **International Journal of Geomechanics**, 2020, 20(2): 4019150.

[29] LI X A, LI L, SONG Y. Characterization of the mechanisms underlying loess collapsibility for land-creation project in Shaanxi Province, China—a study from a micro perspective[J]. **Engineering Geology**, 2018, 249: 77−88.

[30] CAO Q K, JING H X, LI H. Optimization of fly ash foam concrete mix proportion based on response surface methodology[J]. **Bulletin of the Chinese Ceramic Society**, 2024, 43(4): 1427−1435.

[31] PADAVALA S S A B, NOOLU V, PALURI Y, et al. Performance evaluation of concrete blended with industrial and agricultural wastes reinforced with hybrid fibres–a feasibility study[J]. **Scientific Reports**, 2025, 15(1): 6662.

[32] GONG Y F, SONG J X, HE Y L, et al. Value coefficient of polyethylene fiber soil embankment slope based on response surface analysis[J]. **Polymers**, 2022, 14(20): 4295.

[33] LI Yan, LI Tong-lu, HOU Xiao-kun, et al. Prediction of unsaturated permeability curve of compaction loess with pore-size distribution curve and its application scope[J]. **Rock and Soil Mechanics**, 2021, 42(9): 2395−2404.

[34] TULLER M, OR D. Water films and scaling of soil characteristic curves at low water contents[J]. **Water Resources Research**, 2005, 41(9): W09403.